

# Modelling of physical systems with a Hopf bifurcation using mechanistic models and machine learning

K. H. Lee<sup>\*1</sup>, D. A. W. Barton<sup>†1</sup>, and L. Renson<sup>‡2</sup>

<sup>1</sup>Department of Engineering Mathematics, University of Bristol, UK

<sup>2</sup>Department of Mechanical Engineering, Imperial College London, UK

## Abstract

We propose a new hybrid modelling approach that combines a mechanistic model with a machine-learned model to predict the limit cycle oscillations of physical systems with a Hopf bifurcation. The mechanistic model is an ordinary differential equation normal-form model capturing the bifurcation structure of the system. A data-driven mapping from this model to the experimental observations is then identified based on experimental data using machine learning techniques. The proposed method is first demonstrated numerically on a Van der Pol oscillator and a three-degree-of-freedom aeroelastic model. It is then applied to model the behaviour of a physical aeroelastic structure exhibiting limit cycle oscillations during wind tunnel tests. The method is shown to be general, data-efficient and to offer good accuracy without any prior knowledge about the system other than its bifurcation structure.

**Keywords** Hopf bifurcation, Machine learning, Hybrid mechanistic/machine-learned model, Aeroelastic system, Limit cycle oscillations

## 1 Introduction

Limit-cycle oscillations (LCOs) are periodic responses that can be observed in many systems such as aircraft wings [1], wheels [2], machine tools [3], and living cells [4, 5]. *Self-excited* systems are a common source of LCOs and are typically modelled using ordinary differential equations (ODEs) where the variation of a parameter beyond a critical value (a bifurcation point) triggers oscillations.

Deriving a low-dimensional mathematical model that quantitatively captures the onset and amplitude of LCOs is usually a very challenging problem as self-excited systems are typically characterised by the interplay of several physical phenomena. Take, for example, the aforementioned fluid-structure and tyre-ground interactions in wings and wheels, respectively.

For self-excited systems with a Hopf bifurcation, the change in parameter leads to a loss of stability of the equilibrium and the birth of a family of LCOs near the bifurcation point. To analyse the periodic responses of such systems and determine the amplitude of the LCOs, it is customary to reduce the dynamics of the original system near the bifurcation point to a low-dimensional centre manifold. The reduced system is topologically equivalent to the full model, i.e. the vector flows are locally qualitatively identical and there exists a smooth invertible coordinate transformation between them [6]. The hybrid modelling methodology proposed here takes advantage of this equivalence. A low-dimensional normal form model is used to capture the phenomenology of the real system, i.e. its bifurcation structure. A data-driven mapping from this model to the full system is then identified using machine learning (ML) and experimentally measured data (here LCOs).

The use of ML models is attractive because they are theoretically able to represent any continuous functions [7]. However, using traditional ML techniques and models presents a number of difficulties. For

---

\*Corresponding Author: jz18526@bristol.ac.uk

†david.barton@bristol.ac.uk

‡l.renson@imperial.ac.uk

instance, a considerable amount of data is often needed to train ML models [8]. Furthermore, even if such data is available and the obtained ML model accurately represents the training data set, ML models can still fail to generalise to unseen conditions [9] or even fail to capture the fundamental physics of the system [10]. The approach proposed in this paper is inspired by the recent development of scientific machine learning (SciML), which aims at making ML models more interpretable, more consistent with the known laws of physics, and less data-hungry by combining them with mechanistic (i.e. physics-based) models. Examples of SciML approaches include Physics-Informed Neural Networks (PINNs) [11] where a neural network is used to solve and discover partial differential equations (PDEs) while respecting the laws of physics through constraints incorporated into the training cost function. In Refs. [12,13] linear ordinary differential equations (ODEs) were successfully discovered from data using probabilistic machine learning and Gaussian process regression. Universal differential equations (UDEs) [14] are differential equation models combining mechanistic differential equations with universal approximators such as neural networks, Chebyshev expansions, or random forests directly introduced into the model equations.

While existing studies have mostly focused on numerical simulations and a quantitative agreement between time-series at particular parameter values, the approach proposed here aims to capture the bifurcation diagram of a physical system, which requires the accurate prediction of the system’s parameter dependence, its long-term behaviour (here LCOs), and to deal with experimental (i.e. noise-corrupted) measurements. In this context, Beregi et al. [15] combined machine-learnable functions with mechanistic models to capture bifurcation diagrams. The approach proposed here differs in that it uses only the knowledge of the bifurcation structure observed in the experiment. The normal form model and its associated bifurcation structure form the mechanistic model that captures the “*physics*” of the system and underpins the otherwise data-driven model. The hybrid mechanistic/machine-learnt (M/ML) model obtained does not rely on any problem specific variables and is therefore applicable to any system exhibiting the bifurcation structure imposed by the underlying mechanistic model, even without any other physical model available.

Simple parameter sweeps are often enough to reveal such a bifurcation structure, including its supercritical or subcritical nature. The use of a model to capture the type of bifurcation observed in the data is very beneficial as it reduces the amount of data required to train the model and improves the ability of the model to interpolate between data points and even extrapolate outside the range of control parameters used for model training. Moreover, by leveraging the fact that the dynamics of the system evolves on a low-dimensional sub-manifold and using a polar representation, the training of time series requires the time integration of a single one-dimensional ODE, which is computationally much more efficient than other data-driven modelling procedures using numerical integration of the entire model as in [14]. The hybrid M/ML models developed in this paper could be exploited in different ways. For instance, the machine-learnt mapping could be analysed to improve understanding about the physical system and provide new insights into the derivation of more accurate mechanistic models. The proposed models have also the potential to be used as digital twins where the nature of the system is captured qualitatively using the mechanistic part of the model and data is continuously used to refine and evolve the model during the system’s life. Exploring these applications is outside the scope of the paper.

The manuscript is structured as follows. The second section discusses the theoretical background of the proposed modelling approach, and the third section explains the process used to train the data-driven part of the model. In Section 4, the proposed modelling approach is validated numerically on a Van der Pol oscillator and a three-degree-of-freedom aeroelastic model representative of the physical system studied in Section 5. The numerical experiments show that the proposed methodology accurately predicts the phase portrait, bifurcation diagram and time series of the studied systems. Finally, the proposed hybrid modelling approach is successfully validated experimentally in Section 5. The physical system considered is an aerofoil that exhibited LCOs when tested in the wind tunnel. The data exploited in this paper was collected using control-based continuation (CBC) [16–20]. Contrary to conventional parameter sweeps which can only measure stable LCOs, CBC uses feedback control to stabilise, and hence observe unstable LCOs, which can benefit parameter estimation [21,22]. The hybrid M/ML model built with the proposed approach is shown to capture the overall bifurcation structure of the physical system and to reproduce quantitatively the amplitude of both stable and unstable LCOs measured in the experiment.

## 2 Model structure

**Mechanistic model** It is assumed that the physical system of interest can be represented by an unknown continuous-time dynamical system  $(N, \Phi^t)$ , where  $N \subset \mathbb{R}^{n+1}$  with  $n \geq 2$  is the number of states and  $\Phi^t : \mathbb{R}^+ \times N \rightarrow N$  is the evolution of the flow governed by a set of ODEs. The system  $(N, \Phi^t)$  is assumed to undergo a Hopf bifurcation at certain parameter  $\mu = \mu_0$  and the sub-/super-critical nature of the bifurcation is known (or at least identifiable from experimental data). The parameter  $\mu$  is constant over time and taken as one of the dimensions of  $N$ .

There exists a 3-dimensional centre manifold  $M^c$  near the Hopf bifurcation point that can be parametrised as a graph  $\mathbf{M}_{\mathbf{x}}^c$  [23]:

$$\mathbf{M}_{\mathbf{x}}^c = \{(\mathbf{x}, \mathbf{y}) | \mathbf{y} = \mathbf{h}(\mathbf{x})\}, \quad (1)$$

where  $\mathbf{x}$  is the center subspace,  $\mathbf{y}$  is the attracting subspace defined at the equilibrium of  $(N, \Phi_{\text{full}}^t)$ , and  $\mathbf{h}$  is a nonlinear function.  $M^c$  is an attracting invariant manifold in the state-space of the full dynamical system  $(N, \Phi_{\text{full}}^t)$ . The dynamics of the system on the centre manifold is defined as  $(M^c, \Phi_{\text{red}}^t)$ , where  $\Phi_{\text{red}}^t : \mathbb{R}^+ \times M^c \rightarrow M^c$  is the evolution of the flow on the centre manifold  $M^c$ . The system  $(M^c, \Phi_{\text{red}}^t)$  is a reduced order model of  $(N, \Phi_{\text{full}}^t)$  with  $\dim(M^c) \leq \dim(N)$ . The reduced dynamics is usually expressed as  $\dot{\mathbf{x}} = \mathbf{f}(\mathbf{x})$  where  $\mathbf{f}$  is the system's vector field projected onto the centre manifold parametrised by  $\mathbf{x}$ . It is also possible to find a smooth, invertible change of coordinates such that the reduced dynamics can be represented using the modified Hopf normal form

$$\begin{aligned} \dot{u}_1 &= (\mu - \mu_0)u_1 - u_2\Omega(u_1, u_2, \mu) + a_2u_1(u_1^2 + u_2^2) - u_1(u_1^2 + u_2^2)^2, \\ \dot{u}_2 &= (\mu - \mu_0)u_2 + u_1\Omega(u_1, u_2, \mu) + a_2u_2(u_1^2 + u_2^2) - u_2(u_1^2 + u_2^2)^2, \\ \dot{\mu} &= 0, \end{aligned} \quad (2)$$

which can also be written in polar coordinates as

$$\begin{aligned} \dot{r} &= (\mu - \mu_0)r + a_2r^3 - r^5 \\ \dot{\theta} &= \Omega(r, \theta, \mu) \\ \dot{\mu} &= 0. \end{aligned} \quad (3)$$

where  $(u_1, u_2, \mu)$ , or  $(r, \theta, \mu)$ , are the coordinates parameterizing the invariant manifold. The sign of the coefficient  $a_2$  depends on the criticality of the Hopf bifurcation. Fifth-order terms are added to the standard Hopf normal form to introduce a saddle-node bifurcation of periodic orbits and capture the presence of stable LCOs frequently observed in systems with subcritical Hopf bifurcations. For the latter, stable and unstable LCOs coexist for  $\mu \in [\mu_0 - a_2^2/4, \mu_0]$ .  $\Omega$  is an a priori unknown function that governs the speed of the oscillations and that reproduces the time evolution of the data (see Section 3). From Eq. (3), it is clear that the oscillation amplitude  $r$  is independent of the oscillation speed. This observation will be exploited in Section 3 to simplify the ML model training by learning the coordinate mapping and the oscillation speed separately.

Eqs. (2) and (3) are not the only way to represent the dynamics of a system with a Hopf bifurcation followed by a saddle node bifurcation. An alternative parameterization of the invariant manifold, using, for instance,  $\mathbf{x}$  as in Eq. (1), can be used. This would result in a set of ODEs that is different from Eqs. (2) and (3). However, those different reduced systems are topologically equivalent to each other, i.e. one can be transformed to another by a change of coordinates [6]. The choice to take the well-known normal form as a mechanistic model was made to emphasize the nature of the phenomenon targeted by the model.

**Mapping to observations** Following the definition of the mechanistic model (2), a data-driven transformation from the model to the observation is defined. Let's consider the measured observations  $\mathbf{z} = [z_1, \dots, z_m, \mu]^T \in \mathbb{R}^{m+1}$ , where  $m$  is the total number of states observed, and the predicted observations  $\hat{\mathbf{z}} = [\hat{z}_1, \dots, \hat{z}_m, \hat{\mu}]^T \in \mathbb{R}^{m+1}$ . A function  $\mathbf{g}(u_1, u_2, \mu) = \hat{\mathbf{z}}$  can be defined to map the dynamics of the reduced system (2) to the predicted experimental observations  $\hat{\mathbf{z}}$  made on the centre manifold  $M^c$ . The map  $\mathbf{g}$  can be defined as a vector of two functions  $\mathbf{g} = [\mathbf{U}^T, g_\mu]^T$ . The first function,  $\mathbf{U}(u_1, u_2, \mu) = [\hat{z}_1, \dots, \hat{z}_m]^T$ ,

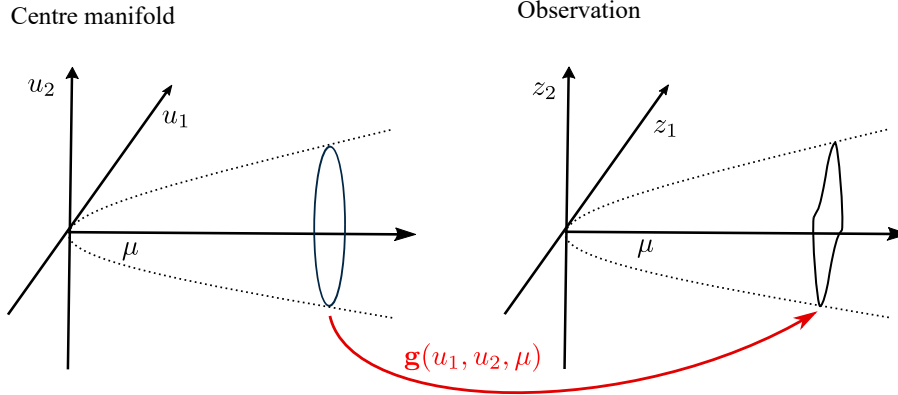


Figure 1: Geometric illustration of the coordinate transformation  $\mathbf{U}_{12}(u_1, u_2, \mu)$  applied to a LCO of a supercritical Hopf bifurcation.

represents the mapping between  $(u_1, u_2, \mu)$  and the observed states. The LCOs in Eq. (2) trace circular trajectories in the plane  $(u_1, u_2)$ . The objective of the mapping  $\mathbf{U}$  is thus to transform these circles into the distorted closed curves observed experimentally (as illustrated in Fig. 1). The second part of the map  $\mathbf{g}$ ,  $g_\mu(u_1, u_2, \mu) = \hat{\mu}$ , represents the mapping between the model parameter  $\mu$  and the predicted observed parameter. In the present and common case where the bifurcation parameter is directly measured during the experiment and not re-scaled, the mapping reduces to a simple projection, i.e.  $g_\mu(u_1, u_2, \mu) = \mu$ .

### 3 Model training

#### 3.1 Closed orbit representation

We assume there exist a pair of coordinates for which the measured LCOs form closed curves that can be parameterised in polar coordinates, i.e. the LCOs form curves that do not self-intersect and have a unique angular parameterisation. This assumption is satisfied in the neighbourhood of the Hopf bifurcation point, and it is assumed that it extends to all the measured LCOs. For convenience, this pair of coordinates is labelled  $(z_1, z_2)$ , while the remaining measured coordinates are  $(z_3, \dots, z_m)$ . The map  $\mathbf{U}$  is split accordingly as  $\mathbf{U} = [\mathbf{U}_{12}^T, \mathbf{U}_{3..m}^T]^T$ .

The map  $\mathbf{U}_{12}$  from the normal form coordinates  $(u_1, u_2, \mu)$  to the predicted observations  $(\hat{z}_1, \hat{z}_2)$  is first sought. The particular challenge associated with finding this first map  $\mathbf{U}_{12}$  is that the correspondence between points  $(u_1, u_2)$  in the normal form coordinates and observations  $(z_1, z_2)$  is initially unknown. Therefore, it is not possible to obtain  $\mathbf{U}_{12}$  by solving a regression problem as input and output data points cannot be paired together. However, once this first map is found, the rest of the map  $\mathbf{U}$  addressing the presence of additional states  $(\hat{z}_3, \dots, \hat{z}_m)$  can be determined easily. This will be discussed later in this section.

**Finding the first mapping** To train  $\mathbf{U}_{12}$ , the idea is to compare continuous representation of the predicted and measured LCOs. This approach has the advantage of avoiding any point-wise comparison between data points and model predictions. The training process starts by taking a user-defined number of points along periodic responses in the normal form coordinates. Those points are mapped to the observation space using the current estimate of the mapping  $\mathbf{U}_{12}$ . Following the coordinate transformation, the closed curves obtained from the transformed trajectories can be directly compared with the measured LCOs. Comparing closed planar curves is a well-established problem in pattern recognition [24, 25], and a popular way to approach this problem is to use a Fourier representation of the curve along the arc-length [26]. However, with such a representation, it is difficult to define a metric between two distinct curves if they do not share at least one point. For this reason, we here consider the simpler approach of directly using a phase-like angle to parameterise the orbit. This assumption is consistent with the normal form model and the closed curves

observed experimentally, that have a much simpler geometry than the one usually investigated in pattern recognition [26]. The polar representation of the planar orbits in terms of amplitude and angle is obtained for measured and predicted curves as

$$R = \sqrt{z_1^2 + z_2^2}, \quad \theta = \tan^{-1} \frac{z_2}{z_1}, \quad \text{and} \quad \hat{R} = \sqrt{\hat{z}_1^2 + \hat{z}_2^2}, \quad \hat{\theta} = \tan^{-1} \frac{\hat{z}_2}{\hat{z}_1}. \quad (4)$$

As the polar representations of the LCOs are assumed to be smooth and periodic, they can be represented as a truncated Fourier series

$$R(\theta) = a_0 + \sum_{k=1}^{n_h} a_k \cos(k\theta) + \sum_{k=1}^{n_h} b_k \sin(k\theta), \quad \text{and} \quad \hat{R}(\hat{\theta}) = \hat{a}_0 + \sum_{k=1}^{n_h} \hat{a}_k \cos(k\hat{\theta}) + \sum_{k=1}^{n_h} \hat{b}_k \sin(k\hat{\theta}), \quad (5)$$

where the number of Fourier modes,  $n_h$ , is assumed to be sufficiently large to have a small approximation error. The shape of the closed curves  $R(\theta)$  and  $\hat{R}(\hat{\theta})$ , are thus represented by vectors of coefficients determined by the Fourier projection  $\Phi(\cdot)$  as  $\Phi(R) : C_p([0, 2\pi], \mathbb{R}) \rightarrow \mathbb{R}^{2n_h+1} = [a_0, \dots, a_{n_h}, b_1, \dots, b_{n_h}]^T$  where

$$a_0 = \frac{1}{2\pi} \int_0^{2\pi} R d\theta, \quad a_n = \frac{1}{\pi} \int_0^{2\pi} R \cos(n\theta) d\theta, \quad b_n = \frac{1}{\pi} \int_0^{2\pi} R \sin(n\theta) d\theta \quad \text{for } n = 1, 2, \dots, n_h. \quad (6)$$

Alternatively, the vector of coefficient can be computed in a least-square sense directly using Eq. (5) and the pseudo inverse [27].

Taking a family of LCOs from the branch emerging at the Hopf bifurcation point, the error between model predictions and the data is given by

$$\Xi_{\mathbf{U}} = \sum_{i=1}^{m_s} \|\Phi(R_i) - \Phi(\hat{R}_i)\| \quad (7)$$

where  $m_s$  is the number of measured LCOs. This measure of the model error is the cost function that is minimised during the training of the coordinate transformation detailed in Section 3.2.

**Mapping to other coordinates** After obtaining  $\mathbf{U}_{12}$ , it is possible to use the inverse transformation  $\mathbf{U}_{12}^{-1}$  to find the points in the normal form coordinates that are associated with the measured data. Considering those points as inputs, it is then straightforward to train the  $m-2$  remaining maps to the output observations  $(z_3, \dots, z_m)$  using standard input-output regression techniques such as kernel ridge regression [28] or neural networks.

Although not explored here, an alternative approach to predict the remaining measured coordinates would be to consider the pair  $(z_1, z_2)$  as so-called ‘*master*’ coordinates and  $(z_3, \dots, z_m)$  as ‘*slave*’ coordinates of the system. Once the master coordinates are obtained from the normal form model using  $\mathbf{U}_{12}$ , a second mapping from the master coordinates to the slave coordinates can be learnt. This second problem is also a regression problem which can be easily solved. This procedure is conceptually similar to the classical centre manifold reduction approach (see Eq. (1)). However, here, the mappings to the master coordinates and between master-slave coordinates are sought based on experimental data. This approach is also completely independent of the bifurcation structure.

More generally, there exist also other approaches to train the overall mapping  $\mathbf{U}$ . For instance, a common parameterisation for the predicted (model) and observed (data) time series could be enforced. Time cannot be used as the oscillation speed  $\Omega$  is trained separately. It is therefore natural to resort to a geometrical parameterisation of the time series in terms of phase-like angles like the one used for the parametrisation of the closed curves. Following a re-parametrisation of the predicted (measured) responses in terms of this phase angle, a one-to-one correspondence between data points in the normal form and observation coordinates can be assumed, and input-output regression performed to identify the mapping associated with each measured coordinate. While this approach appears straightforward, it was found more difficult to generate model predictions at the particular phase angles observed experimentally. As such, interpolation of the model predictions was necessary, which affected the precision of the overall training procedure.

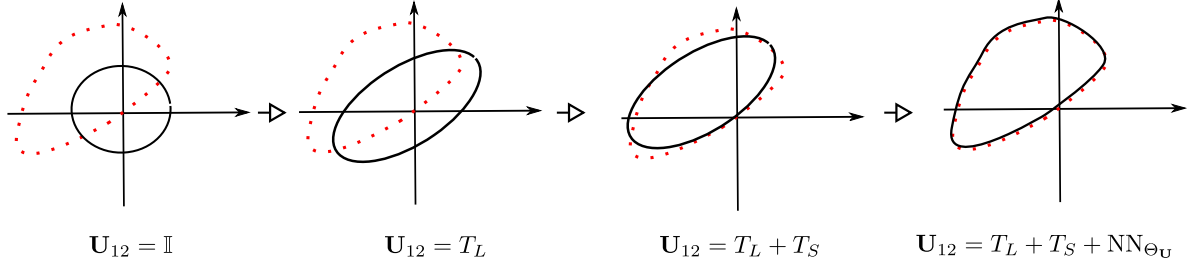


Figure 2: Combined effect of the different components included in the transformation from normal form coordinates  $\mathbf{u}$  to physical space  $\mathbf{z}$ . (—) LCO obtained after transformation. (•) Experimental data.

### 3.2 Functional form of the map

Neural networks provide a flexible approach to model the mapping  $\mathbf{U}_{12}$  [7, 29]. However, it was found that using a neural network alone often leads to mappings that do not preserve the topology of the LCOs. It is therefore advantageous to use a simpler initial transformation that preserves this topology. This transformation has the additional benefits of reducing the complexity of the neural network and simplifying its training. The planar mapping  $\mathbf{U}_{12}(u_1, u_2, \mu) = [\hat{z}_1, \hat{z}_2]^T$  is thus defined as the sum of three separate contributions as

$$\mathbf{U}_{12}(u_1, u_2, \mu) = \underbrace{T_L(u_1, u_2, \mu)}_{\text{Transforms LCO to an ellipse}} + \underbrace{T_s}_{\text{Correction}} + \underbrace{\text{NN}_{\Theta_{\mathbf{U}}}(u_1, u_2, \mu)}_{\text{Correction}}, \quad (8)$$

where

$$T_L(u_1, u_2, \mu) = \begin{bmatrix} l_{11} & l_{12} & l_{13} \\ l_{21} & l_{22} & l_{23} \\ l_{31} & l_{32} & l_{33} \end{bmatrix} \begin{bmatrix} u_1 \\ u_2 \\ \mu \end{bmatrix} \quad \text{and} \quad T_s = \begin{bmatrix} s_1 \\ s_2 \end{bmatrix}. \quad (9)$$

The linear transformation performed by  $T_L(u_1, u_2, \mu) = [\hat{z}_1, \hat{z}_2]^T$  stretches and rotates the closed curves. This transformation includes nine unknown parameters  $l_{ij}$  that will be estimated using experimental data. The transformation matrix must be nonsingular. The coordinate transformation  $T_s(u_1, u_2, \mu) = [\hat{z}_1, \hat{z}_2]^T$  applies a rigid translation of the trajectories and requires two additional parameters  $s_1, s_2$ . Finally,  $\text{NN}_{\Theta_{\mathbf{U}}}(u_1, u_2, \mu) = [\hat{z}_1, \hat{z}_2]^T$  is a neural network with unknown weight vector  $\Theta_{\mathbf{U}}$ .

Including  $T_L$  and  $T_s$  explicitly in  $\mathbf{U}_{12}$  can be interpreted as introducing additional physics or knowledge into the definition of the coordinate transformation. Indeed, shifting and rescaling coordinates must be performed to transform the orbits from the space of the normal form model to the space of the physical system and this operation is commonly performed in normal form calculations in bifurcation analysis. With this approach, the neural network model,  $\text{NN}_{\Theta_{\mathbf{U}}}$ , can be viewed as a “small” correction to the initial transformation performed by  $T_L + T_s$  (Fig. 2).

### 3.3 Oscillation speed

The flow velocity on a LCO trajectory is defined by the general expression

$$\Omega(r \cos \theta, r \sin \theta, \mu) = \omega_0 + \text{NN}_{\Theta_{\Omega}}(r, \mu)^T [1, \cos \theta, \dots, \cos n_h \theta, \sin \theta, \dots, \sin n_h \theta]^T, \quad (10)$$

where the first term,  $\omega_0$ , represents the fundamental oscillation frequency. The second term provides a periodic correction to this fundamental frequency in order to capture state and parameter dependencies. While this general correction term is particularly useful for capturing systems where multiple timescales occur within the LCO, it can be significantly simplified for systems where only one frequency dominates the response (see Section 4).

Following the training of the coordinate transformation,  $\Omega$  is trained by minimising the prediction error between predicted and observed time series. To generate time series from the model, suitable initial conditions

in the normal form coordinates that corresponds to the initial measured data must be obtained. One approach to find the initial conditions  $\mathbf{u}^i(t_1)$  would be to solve

$$[\mathbf{u}^i(t_1), \mu_i] - \mathbf{g}^{-1}(\mathbf{z}^i(t_1), \mu_i) = 0 \quad (11)$$

where  $t_1$  represents the first time instant in the time series. However, model inaccuracies and measurement noise perturbs the initial point,  $\mathbf{u}^i(t_1)$ , away from the trajectory of the LCO predicted at the parameter value  $\mu_i$ . While this is not a significant problem when training stable LCOs; it becomes an issue for unstable LCOs as the numerical integration of the initial value problem will not approach the trajectory of LCOs. The approach followed to solve this issue is to find the initial conditions  $\mathbf{u}^i(t_1)$  for which the model prediction  $(\hat{z}_1^i, \hat{z}_2^i) = \mathbf{U}_{12}(\mathbf{u}^i(t_1), \mu_i)$  has the same phase angle  $\theta$  as the initial conditions of the measured signal. The initial conditions in the normal form coordinates,  $\mathbf{u}^i(t_1)$ , are thus found by solving

$$\text{ang} \circ \mathbf{U}_{12}(\mathbf{u}^i(t_1), \mu_i) - \text{ang} \circ \mathbf{z}^i(t_1) = 0, \quad (12)$$

where  $\text{ang} : (x, y) \mapsto \tan^{-1}(y/x)$  measures the phase angle of the vector  $[x, y]^T$ . Eq. (12) can be solved using Newton method. Note that the initial conditions in the normal form coordinates cannot be set directly to the phase angle found in the data because the mapping  $\mathbf{U}_{12}$  does not necessarily preserve this angle.

Once the initial conditions have been determined, the polar form of the normal form model is considered for the numerical integration. In this case, only the second equation of Eq. (3) needs to be integrated as the LCOs correspond to fixed points of the first equation. Only integrating the second equation has also the advantage of avoiding any numerical instability issues even on the unstable solutions. Indeed, this second equation corresponds to the direction of the velocity vector, i.e. the direction vector of the trivial Floquet multiplier that is equal to unity.

The parameters  $\omega_0$  and  $\Theta_\Omega$  defining the oscillation speed  $\Omega$  are then determined by minimizing the cost function

$$\Xi_\Omega = \sum_{i=1}^{m_s} \sum_j \|\mathbf{U}_{12}(\mathbf{u}^i(t_j), \mu_i) - \mathbf{z}_i(t_j)\|, \quad (13)$$

### 3.4 Learning stages

The model training is a three-stage process. The parameters of the linear transformations  $T_L$  and  $T_s$  are found first by minimising  $\Xi_U$ . An approximate value of the bifurcation parameter value  $\mu_0$  is used during that process. After the training of the linear transformation, the LCOs in the normal-form space can be mapped to ellipses that are “close” to the measured trajectories. During the second training step, the parameters of  $\text{NN}_{\Theta_U}$  and more precise values for  $\mu_0$  and  $a_2$  are found by further minimising  $\Xi_U$ . The linear transformation parameters are kept constant during this process. The third training step is to find the parameters associated with the oscillation speed  $\Omega$ , i.e.  $\omega_0$  and  $\Theta_\Omega$ , by minimizing  $\Xi_\Omega$ .

Traditional deep learning packages such as PyTorch [30] and Flux.jl [31] can be used to train  $\mathbf{U}$  and the other model parameters using optimisation techniques such as stochastic gradient decent method [32, 33]. For  $\Omega$ , the package DiffEqFlux.jl [14] which uses stochastic gradient descent methods on the solutions of differential equations [34, 35] was used.

## 4 Numerical demonstration

In this section, the method developed in Sections 2 and 3 is demonstrated numerically on a Van der Pol oscillator and a 3-degree-of-freedom model of an aerofoil undergoing aeroelastic oscillations. The synthetic data used for model training is noise-free and was obtained using time integration. Demonstration on real experimental data is carried out in Section 5.

## 4.1 Van der Pol oscillator

The equations governing the dynamics of the Van der Pol oscillator are

$$\begin{aligned}\frac{dz_1}{dt} &= z_2, \\ \frac{dz_2}{dt} &= 2\mu z_2 - z_1^2 z_2 - z_1,\end{aligned}\tag{14}$$

where the states  $(z_1, z_2)$  and the control parameter  $\mu$  are all assumed to be measured directly. For this example, a supercritical Hopf bifurcation occurs at  $\mu_0 = 0$  and only stable LCOs exist. As such, the parameter  $a_2$  of the mechanistic model (2) is set equal to  $-1$  and the fifth-order terms are removed. Training data is generated for six different parameter values  $\mu = (0.1, 0.28, 0.46, 0.64, 0.82, 0.1)$ . At each parameter values, the oscillator response is simulated over 10 seconds using initial conditions on the LCOs (i.e. there are no transient in the data) and a sampling time of  $0.02$  s. This represents 500 samples per time series, and hence 3000 samples for the whole training data set.

Following the procedure outlined in Section 3, the coordinate transformation is trained first by minimising  $\Xi_{\mathbf{U}}$ . The NN used within  $\mathbf{U}$  consists of three inputs, two hidden layers each with 32 neurons and hyperbolic tangent activation functions, and two outputs. 300 iterations in ADAM [36] with a learning rate of 0.01 followed by 1000 BFGS [37] iterations with a  $10^{-5}$  learning rate were necessary to estimate the NN parameters  $\Theta_{\mathbf{U}}$ . A comparison between the bifurcation diagrams of the real and identified models shows that the hybrid M/ML model accurately captures the system's topological features (Fig. 3(a)). Phase portraits are shown in Figs. 3(b-1)–(d-1). They further demonstrate that an accurate transformation from the normal-form coordinates to the physical coordinates is achieved for the range of parameter values considered. The parameter value at the bifurcation point was estimated at  $\mu = 0.02$ , which is very close to the actual value 0.

Following the training of the coordinate transformation,  $\Omega$  is estimated. The  $\text{NN}_{\Theta_{\Omega}}$  in model Eq. (10) is set to include three inputs, two hidden layers each with 32 neurons and hyperbolic tangent activation functions, and 13 outputs ( $n_h = 10$ ). The model parameters are estimated by minimizing  $\Xi_{\Omega}$ . The training was performed using 2000 iterations in ADAM with a learning rate of 0.01 followed by 1000 BFGS iterations with a  $10^{-5}$  learning rate were necessary. Figs. 3(b-2)–(d-2) show a very good agreement between the time series of the reference and identified models. As the bifurcation parameter increases, the time scale separation becomes more pronounced and errors become noticeable in the transition between the fast and slow portions of the time series (Fig. 3(d-2)). Similar observations can be made for the other state (not shown for conciseness).

## 4.2 Aeroelastic model

A 3-DOF aeroelastic system [38] is now considered to demonstrate numerically the proposed method. This model is qualitatively representative of the physical system tested in Section 5. The equations of motion of this system are

$$\mathbf{M}\ddot{\mathbf{x}} + \mathbf{D}\dot{\mathbf{x}} + \mathbf{K}\mathbf{x} + \mathbf{N}(\alpha) = 0,\tag{15}$$

where

$$\mathbf{M} = \begin{bmatrix} m_T + \pi\rho b^2 & m_w x_{\alpha} b - a\pi\rho b^3 & 0 \\ m_w x_{\alpha} b - a\pi\rho b^3 & I_{\alpha} + \pi(1/8 + a^2)\rho b^4 & 0 \\ 0 & 0 & 1 \end{bmatrix},\tag{16a}$$

$$\mathbf{D} = \begin{bmatrix} c_h + 2\pi\rho b U \hat{c} & (1 + \hat{c}(1 - 2a))\pi\rho b^2 U & 2\pi U^2 b(c_1 c_2 + c_3 c_4) \\ -2\pi(a + 1/2)\rho b^2 \hat{c} U & c_{\alpha} + (1/2 - a)(1 - \hat{c}(1 + 2a))\pi\rho b^3 U & -2\pi\rho b^2 U^2(a + 1/2)(c_1 c_2 + c_3 c_4) \\ -1/b & a - 1/2 & (c_2 + c_4)U/b \end{bmatrix},\tag{16b}$$

$$\mathbf{K} = \begin{bmatrix} k_h & 2\pi\rho b U^2 \hat{c} & 2\pi U^3 c_2 c_4 (c_1 + c_3) \\ 0 & k_{\alpha} - 2\pi(1/2 + a)\rho \hat{c} b^2 U^2 & -2\pi\rho b U^3 (a + 1/2) c_2 c_4 (c_1 + c_3) \\ 0 & -U/b & c_2 c_4 U^2 / b^2 \end{bmatrix},\tag{16c}$$



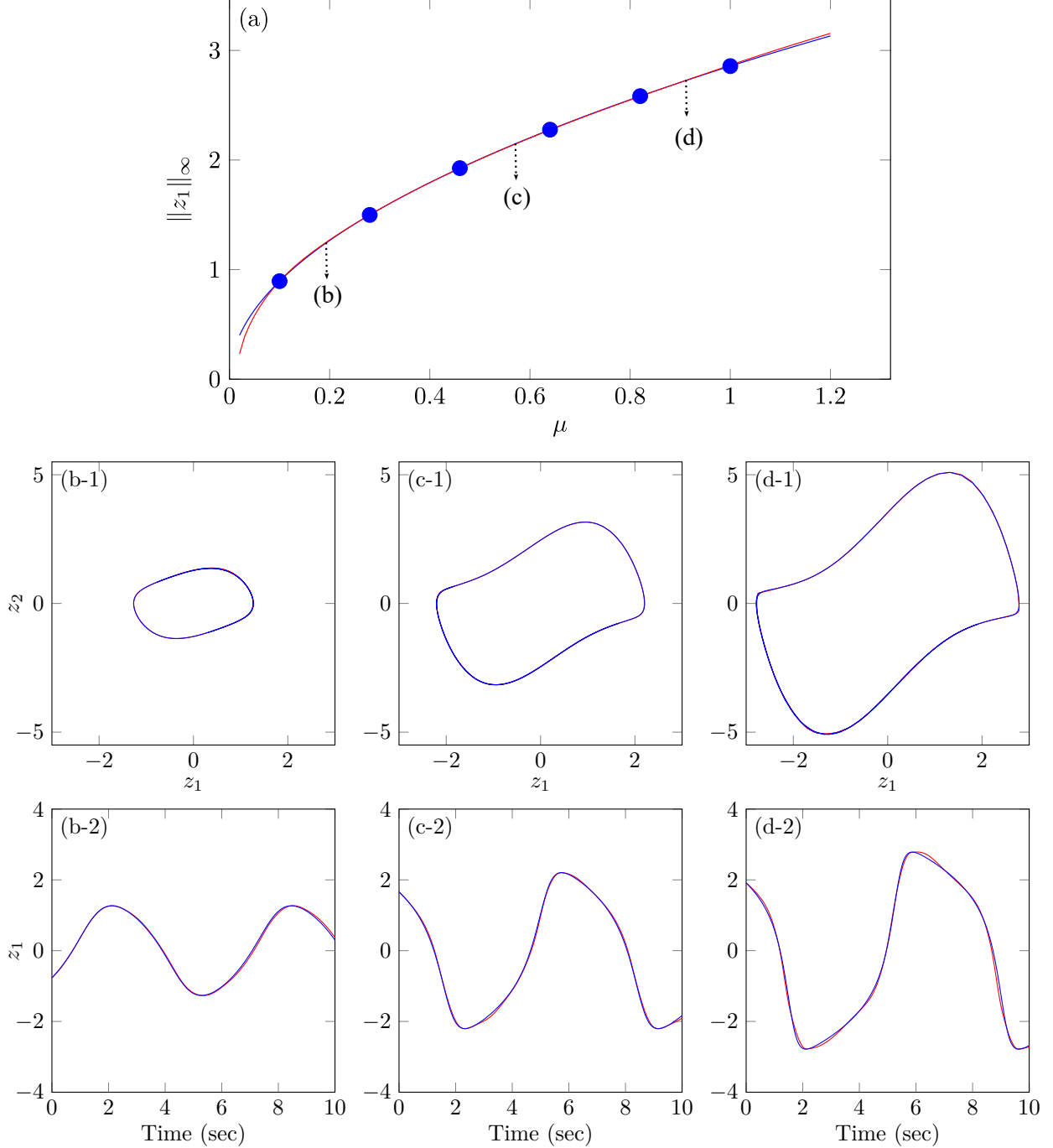


Figure 3: Comparison between the Van der Pol model (—) and the hybrid M/ML model (—). (a) Bifurcation diagram where (●) are the LCOs used for model training. (b-1–d-1) Phase portraits and (b-2–d-2) time-series at the untrained locations reported on the bifurcation diagram.

$\hat{c} = c_0 - c_1 - c_3$  and  $\mathbf{N}(\alpha) = [0, k_{\alpha 2}\alpha^2 + k_{\alpha 3}\alpha^3, 0]^T$ . The meaning of the parameters and their values used are given in Table 1. The bifurcation parameter  $\mu$  represents here the wind velocity.  $h$  and  $\alpha$  stand for the heave displacement and the pitch angle, respectively.

This system has a subcritical Hopf bifurcation followed by saddle-node bifurcation of periodic orbits. The training data set includes four LCOs recorded on the stable branch, and four LCOs recorded on the unstable

Parameter	Value	Description
$U$	0–25	Airspeed (m/s)
$b$	0.15	Wing semi-chord (m)
$a$	−0.5	Position of elastic axis relative to the semi-chord (nd)
$\rho$	1.204	Air density (kg/m <sup>3</sup> )
$m_w$	5.3	Mass of the wing (kg)
$m_T$	16.9	Mass of wing and support (kg)
$I_\alpha$	0.1726	Wing moment of inertia about elastic axis (kg m <sup>2</sup> )
$c_\alpha$	0.5628	Pitch linear damping coefficient (kg m <sup>2</sup> /s)
$c_h$	15.443	Heave linear damping coefficient (kg/s)
$k_\alpha$	54.1162	Pitch linear stiffness (N/rad)
$k_{\alpha 2}$	751.6	Pitch quadratic nonlinear stiffness (N/rad <sup>2</sup> )
$k_{\alpha 3}$	5006.7	Pitch cubic nonlinear stiffness (N/rad <sup>3</sup> )
$k_h$	3529.4	Heave linear stiffness (N/m)
$x_\alpha$	0.234	Distance between center of gravity and elastic axis (nd)
$c_{0,\dots,4}$	(1, 0.1650, 0.0455, 0.335, 0.3)	Aeroelastic coefficients

Table 1: Descriptions of the parameters of Eq. (15) and their values where applicable. Non-dimensional units are indicated by ‘nd’.

branch. As further discussed in Section 5, in an experiment, stable and unstable LCOs can be directly measured using control-based continuation [39, 40]. Here, the unstable LCOs were obtained by simulating the model Eq. (15) under proportional-derivative feedback control to reproduce the process followed for the experimental tests in Section 5. Each time series is recorded for one second with a sampling time of 0.001 s.

For this example,  $\text{NN}_{\Theta_{\mathbf{U}}}$  has two inputs, two hidden layers each with 21 neurons and hyperbolic tangent activation functions, and three linear outputs. 400 iterations in ADAM with a learning rate of 0.01 were necessary to estimate the NN parameters  $\Theta_{\mathbf{U}}$ . Fig. 4(left) shows that the linear transformation allows the coordinate transformation to capture the overall orientation and size of the LCO, and Fig. 4(right) shows that  $\text{NN}_{\Theta_{\mathbf{U}}}$  further improves the accuracy of this coordinate transformation, leading to an excellent visual agreement between the LCO of the hybrid M/ML and reference models.

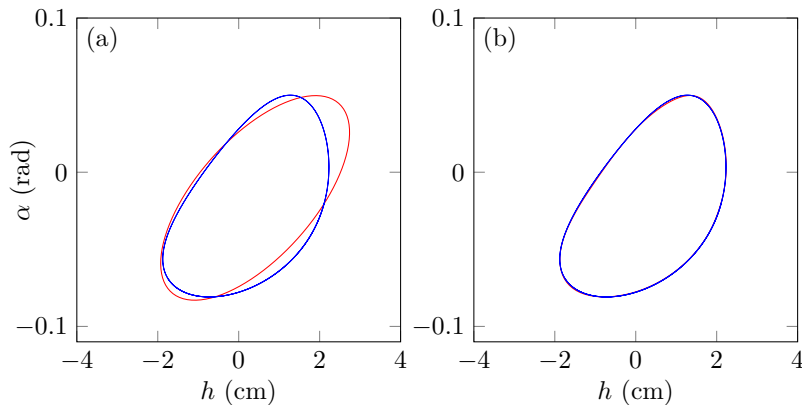


Figure 4: Comparison between the phase portraits of the aeroelastic model (—) and the hybrid M/ML model (—) for a stable LCO at  $\mu = 15.5$  m/s. Coordinate transformation (a) without and (b) with the neural network.

Fig. 5(a) shows there is an excellent agreement between the bifurcation diagrams computed from the reference and hybrid M/ML models. The bifurcation diagram of the trained model was computed by transforming 100 equi-spaced points on the periodic solutions of the normal-form model using  $\mathbf{U}$ . The identified values of the Hopf bifurcation point,  $\mu_0$ , and the saddle-node bifurcation point,  $a_2$ , are 18.28 m/s and 3.64,

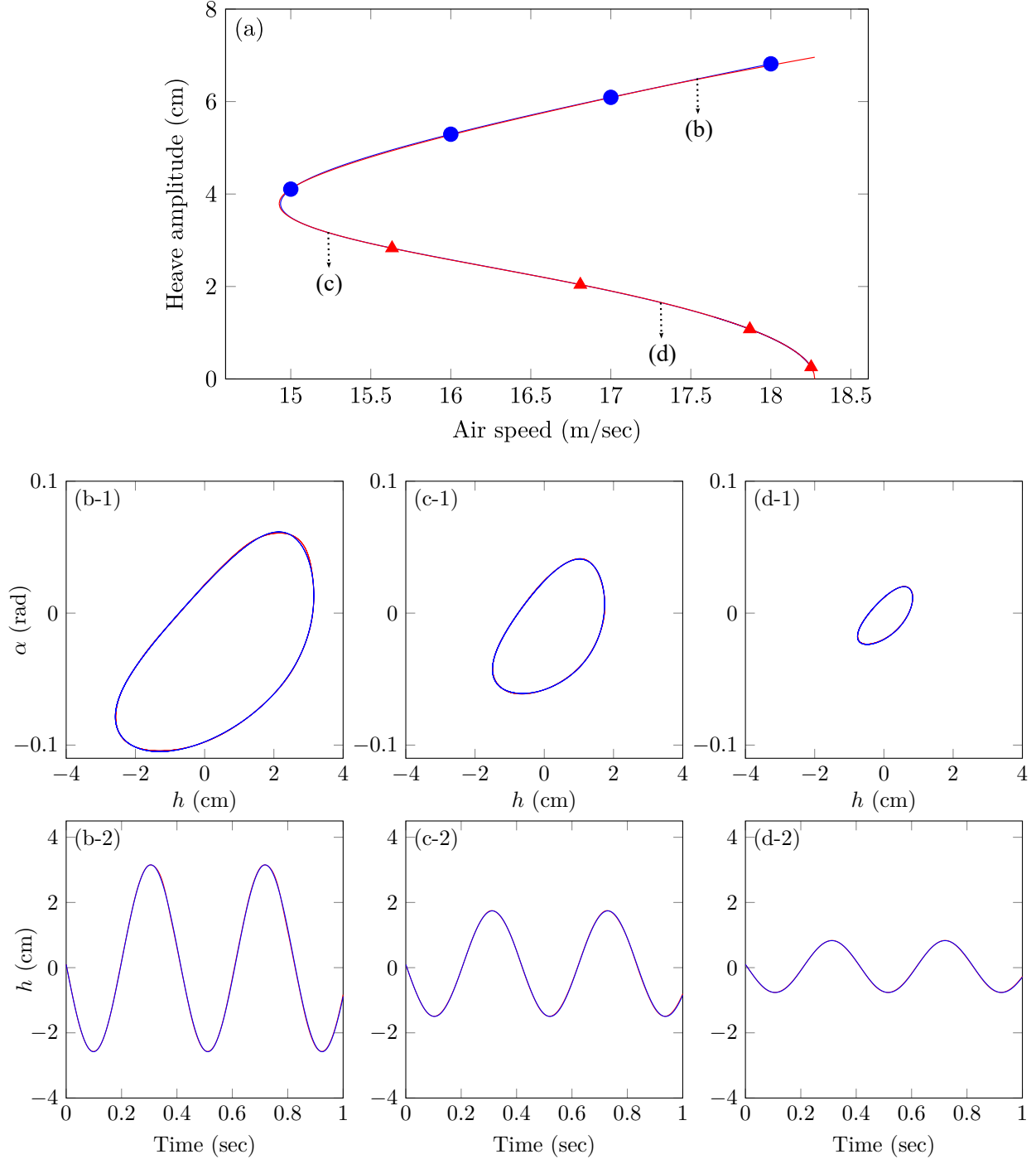


Figure 5: Comparison between the aeroelastic model (—) and the hybrid M/ML model (—). (a) Bifurcation diagram (●) are stable LCOs and (▲) are unstable LCOs used for model training) (b-1–d-1) Phase portraits and (b-2–d-2) time-series at the locations reported on the bifurcation diagram.

respectively. This is in excellent agreement with the model values  $\mu_0 = 18.28 \text{ m/s}$  and  $a_2 = 3.65$ . The phase portrait of the trained model shows good agreement with the model for both stable and unstable LCOs (Figs. 5(b-1)–(d-1)).

The oscillation speed  $\Omega$  is modelled using Eq. (10). For this example, only the constant term in the

Fourier expansion is kept such that  $\Omega(\mathbf{u}, \mu) = \omega_0 + \text{NN}_{\Theta\Omega}(\mathbf{u}, \mu)$ . The neural network consist of three inputs, two hidden layers with 31 neurons each and a hyperbolic tangent activation functions, and one linear output. 300 iterations in ADAM with a learning rate of 0.01 followed by 1000 BFGS iterations with a 0.001 learning rate were necessary to train  $\Omega$  by minimizing  $\Xi_{\Omega}$ . Figs. 5(b-2)–(d-2) show that the model captures the overall time series and frequency of the LCO for the range of wind velocities considered.

## 5 Experimental demonstration on an aeroelastic structure

The method developed in this paper is now demonstrated on a physical aeroelastic system.

### 5.1 Experimental set-up and data collection

The rig is shown in Figure 6. It comprises a NACA-0015 wing profile rigidly attached to a stainless steel shaft, supported at both ends by rotational bearings mounted on supporting plates that are constrained to move vertically by a linear bearing system. The structure has two mechanical degrees of freedom: one in pitch (rotational motion) and one in heave (vertical motion). In the heave direction, linear springs are connected between the supporting plates and the outer frame. In the pitch direction, torsional springs are connected between the shaft and the supporting plates. Both sets of springs provide approximately linear restoring forces in their respective directions. In the pitch direction there are additional leaf springs connecting the shaft and the supporting plates; these leaf springs provide a hardening nonlinearity, mimicking potential interface effects at the root of the aerofoil. The dimensions of the flutter rig are such that the wing profile fits in the principal section of the University of Bristol’s low-turbulence wind tunnel; the supporting plates and outer frame lie outside it (see Figure Fig. 6(b)). The reader is referred to [39] for further details about the dimensions of the system.

Control-based continuation was exploited to measure the stable and unstable LCOs of the system directly during the wind tunnel tests. The control forces are applied in the heave direction by use of an APS 113 electro-seis long-stroke electrodynamic shaker connected by a flexible stinger to one of the supporting plates. The experiment is instrumented with an Omron ZX1-LD300 laser displacement sensor to measure the heave motion, and an RLS AksIM 18 bit absolute magnetic encoder fitted on the shaft to capture the pitch motion. The wind speed was directly provided by the wind tunnel control system. Real-time control and data acquisition is performed using a Beaglebone Black single-board computer equipped with an analogue IO cape (18 bit ADC and 16 bit DAC) operating at a sample rate of 5 kHz [41]. The reader is referred to [39] for further details about the experimental set-up and the CBC method.

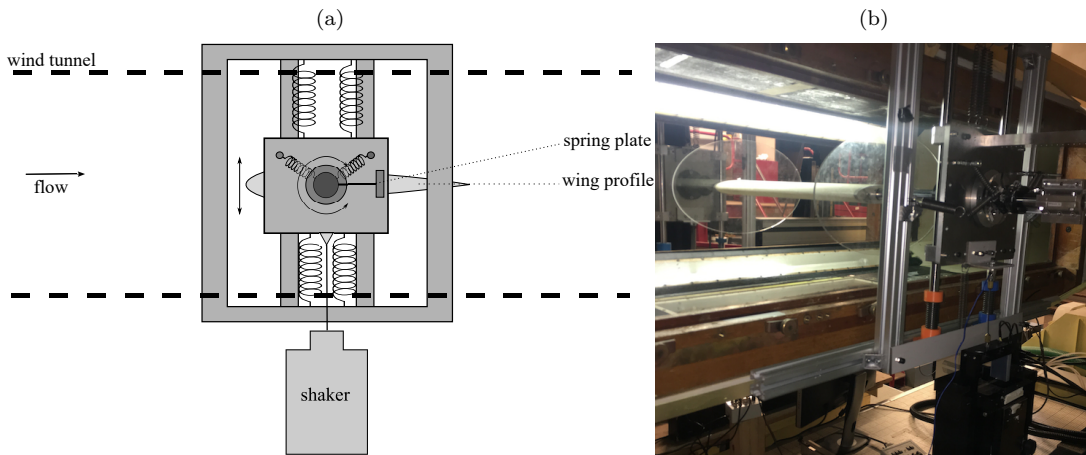


Figure 6: Aeroelastic rig. (a) Schematic. (b) Picture of the rig fitted to the University of Bristol’s low-turbulence wind tunnel.

## 5.2 The hybrid M/ML model

The dynamics of this aeroelastic system is characterised by a subcritical Hopf bifurcation followed by a saddle-node bifurcation of cycles. The mechanistic model used within the hybrid model is therefore the one presented in Eq. (2) and already used in Section 4.2. The training data sets includes four stable LCOs measured at  $\mu = (14.9, 15.6, 16.5, 17.3) \text{ m/s}$ , and three unstable LCOs measured at  $\mu = (14.9, 15.6, 16.5) \text{ m/s}$ . Time series includes 6000 time points per LCOs, which represents approximately 12 oscillation periods. To train the oscillation speed, time series were down sampled to 1000 samples to reduce the computational cost of the training.

For the coordinate map  $\mathbf{U}_{12}$ , a neural network  $\text{NN}_{\Theta_{\mathbf{U}}}$  with three inputs, two outputs and two hidden layers each with 11 neurons and hyperbolic tangent activation functions was used. A first 1000 iterations with ADAM using a 0.01 learning rate followed by 3000 BFGS iterations with a 0.0001 learning rate were necessary to minimize  $\Xi_{\mathbf{U}}$  and find  $\mu_0$ ,  $a_2$  and the network parameters  $\Theta_{\mathbf{U}}$ .

Fig. 7 compares the bifurcation diagram of the hybrid M/ML model with the LCOs measured experimentally. A qualitatively good agreement with the data is obtained despite the limited number of LCOs used for model training. The Hopf bifurcation point is estimated at  $\mu_0 = 17.67 \text{ m/s}$  and the saddle-node bifurcation point at  $14.66 \text{ m/s}$ . Overall, the trained model accurately predicts the phase portrait of the stable and unstable LCOs, as shown in Fig. 8. In the phase portraits, the line associated with the experimentally measured LCOs appears thicker than the one from model predictions. This is an illusion that comes from the presence of multiple oscillation periods in the recorded data and the unavoidable differences that exist between periods due to the presence of noise in the measurements.

For the identification of  $\Omega$ , a similar model to the one used in Section 4.2 is considered. The neural network  $\text{NN}_{\Theta_{\Omega}}(\mathbf{u}, \mu)$  includes three inputs, a single linear output and two hidden layers with 21 neurons each and hyperbolic tangent activation functions. 500 iterations in ADAM with a learning rate of 0.01 followed by 400 BFGS iterations with a 0.001 learning rate were necessary to minimize  $\Xi_{\Omega}$ . The time series presented in Fig. 9 show that the model captures the frequency of the measured LCOs. The amplitude error visible in the bifurcation diagram is also clearly visible in the time series.

One potential issue with ML model training is overfitting. This is illustrated in Fig. 10 where the model was trained using different initial parameter values and different hyperparameters (number of iterations and learning rate). While the overall model prediction error is small at the data points, the model presents a large variability between them which is symptomatic of overfitting. To reduce overfitting and obtain the results presented in Figures 7 – 9, some hyper-parameters, such as the number of iterations, were manually tuned. Approaches that promote parameter sparsity [42] or a formal optimisation of the hyperparameters [43] were not carried out due to the associated computational costs and the overall lack of data. Note that, the use of physics — here, through the model structure (2) and the use of linear transformations in  $\mathbf{U}_{12}$  — can also be viewed as a regularisation techniques that reduces ML model complexity and hence helps in reducing overfitting.

To assess the robustness of the identified model with respect to the training data, the model training was also performed with four different data sets, each with one of the LCO data points removed. This approach is inspired by the leave-one-out cross-validation technique and chosen due to the small number of data points available in the parameter space. Fig. 11 shows the bifurcation diagrams obtained after removing the different data points. The colour of the bifurcation curve matches the colour of the data point that was removed from the training data set. The dashed black bifurcation curve was obtained by including all the data points in the training set. The phase portraits and time series shown in Fig. 11 illustrate the performance of the model at the removed data point. While most bifurcation curves appear similar, removing the stable LCO in blue appears to have a significant influence on the location of the saddle-node bifurcation and more generally on the bifurcation curve in that area. This also affects the quality of the oscillation speed model  $\Omega$ , which is unable to capture the LCO oscillation frequency adequately (see Fig. 11(c-2)). Overall this results suggest that sufficient training data near bifurcation points (saddle-node and Hopf) is needed to build a robust model.

Fig. 12 presents the trained mapping  $\mathbf{U}_{12}$ . Fig. 12(a, b) show the transformation  $\mathbf{U}_{12}$  for  $\mu = 15.0$ , and Fig. 12(c, d) show the transformation  $\mathbf{U}_{12}$  for  $\mu = 17.5 \text{ m/s}$ . The blue dotted lines and the red solid lines correspond to the unstable and stable LCOs, respectively. The coordinate transformations are smooth transformation and locally invertible. The visible curvature shows that the transformations are also

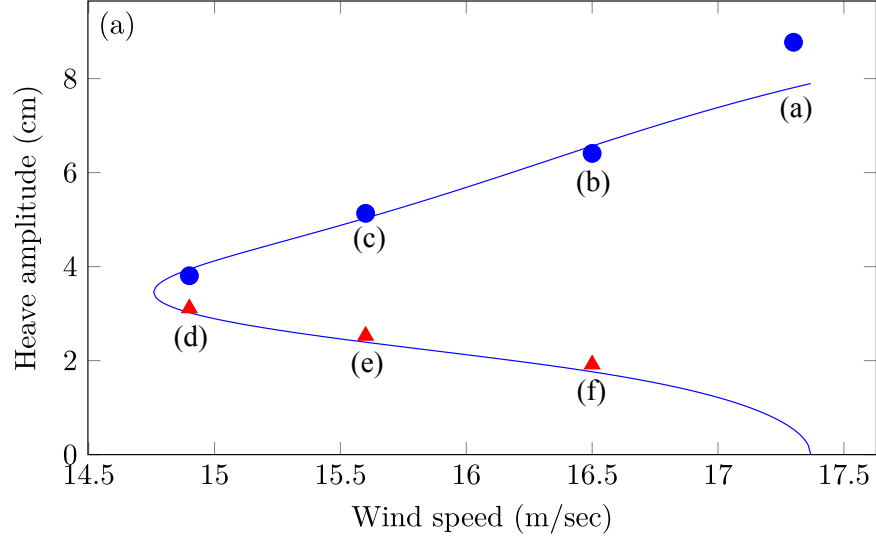


Figure 7: Comparison between the bifurcation diagram obtained from the hybrid M/ML model with increased model accuracy (—) and the stable (●) and unstable (▲) LCOs used for model training. Labels (a)-(f) denote the corresponding phase portraits and time series plots in Fig. 8 and Fig. 9, respectively.

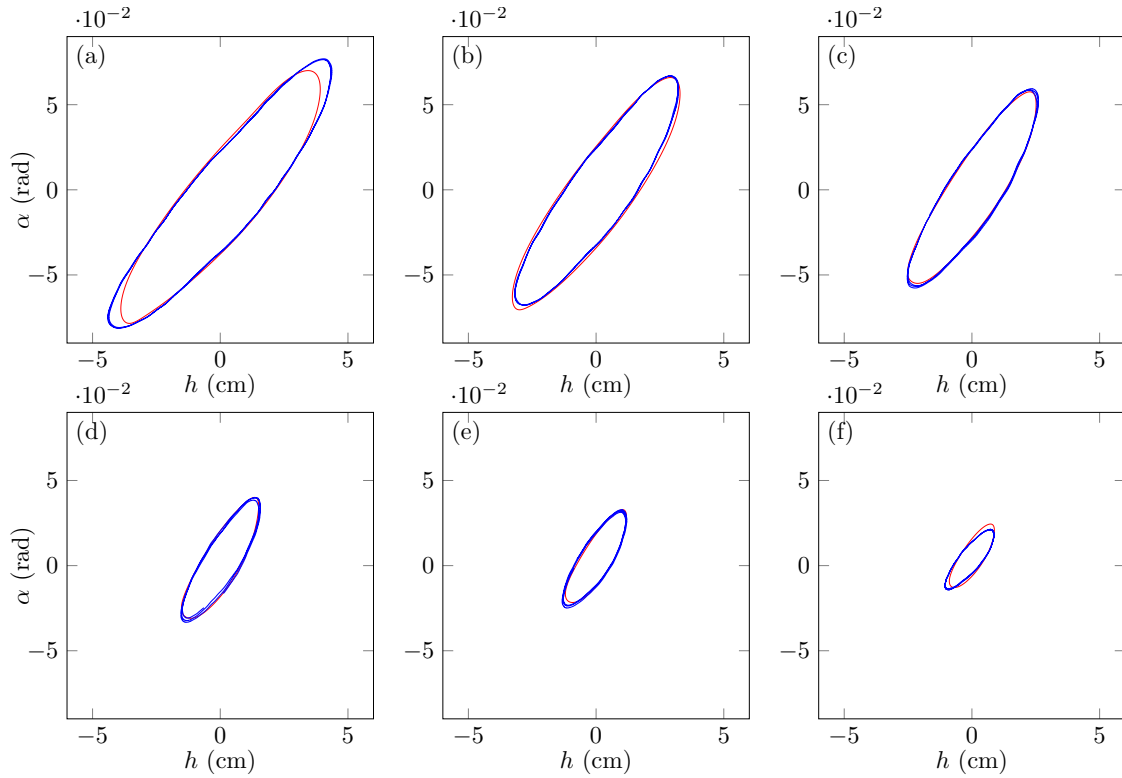


Figure 8: Comparison of phase portraits between the measured LCOs (—) and the hybrid M/ML model (—). (a) stable LCO at wind speed 17.3 m/sec, (b) stable LCO at wind speed 16.5 m/sec, (c) stable LCO at wind speed 15.6 m/sec, (d) unstable LCO at wind speed 14.9 m/sec, (e) unstable LCO at wind speed 15.6 m/sec and (f) unstable LCO at wind speed 16.5 m/sec.

nonlinear. As discussed in Section 3.2, the presence of an initial linear coordinate transformation in (8) was

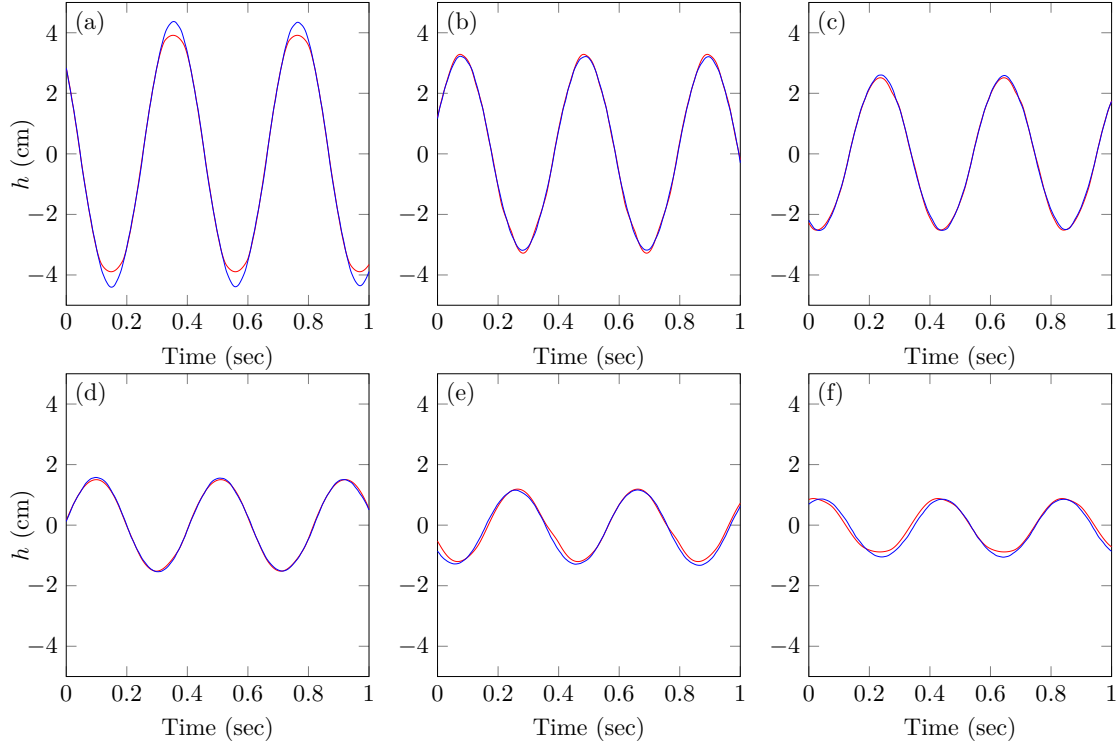


Figure 9: Comparison of heave time series between the measured LCOs (—) and the hybrid M/ML model (—). (a) stable LCO at wind speed 17.3 m/sec, (b) stable LCO at wind speed 16.5 m/sec, (c) stable LCO at wind speed 15.6 m/sec, (d) unstable LCO at wind speed 14.9 m/sec, (e) unstable LCO at wind speed 15.6 m/sec and (f) unstable LCO at wind speed 16.5 m/sec.

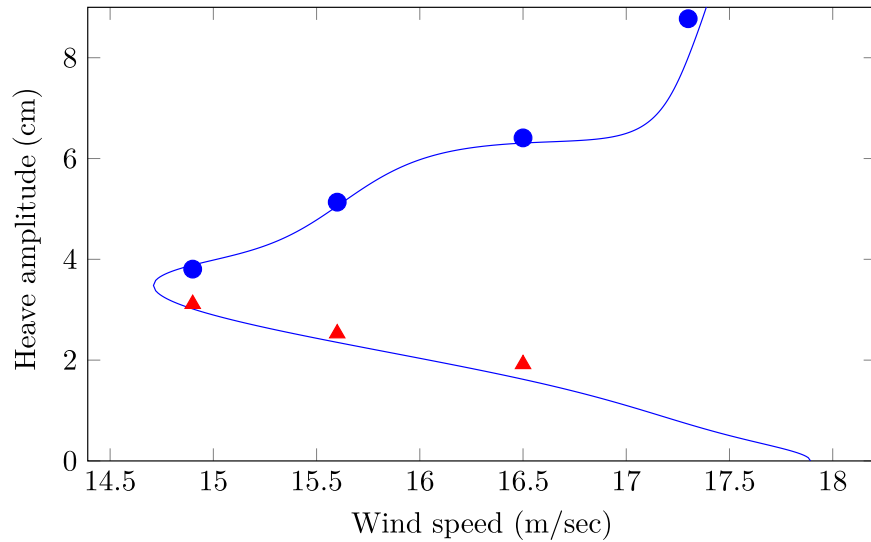


Figure 10: Illustration of model overfitting. Bifurcation diagram obtained from the hybrid M/ML model (—), stable (●) and unstable (▲) LCOs used for model training.

essential. A NN alone was unable to produce topologically equivalent closed curves and obtain a locally invertible transformation near the bifurcation point. Models with significant overfitting, such as the one

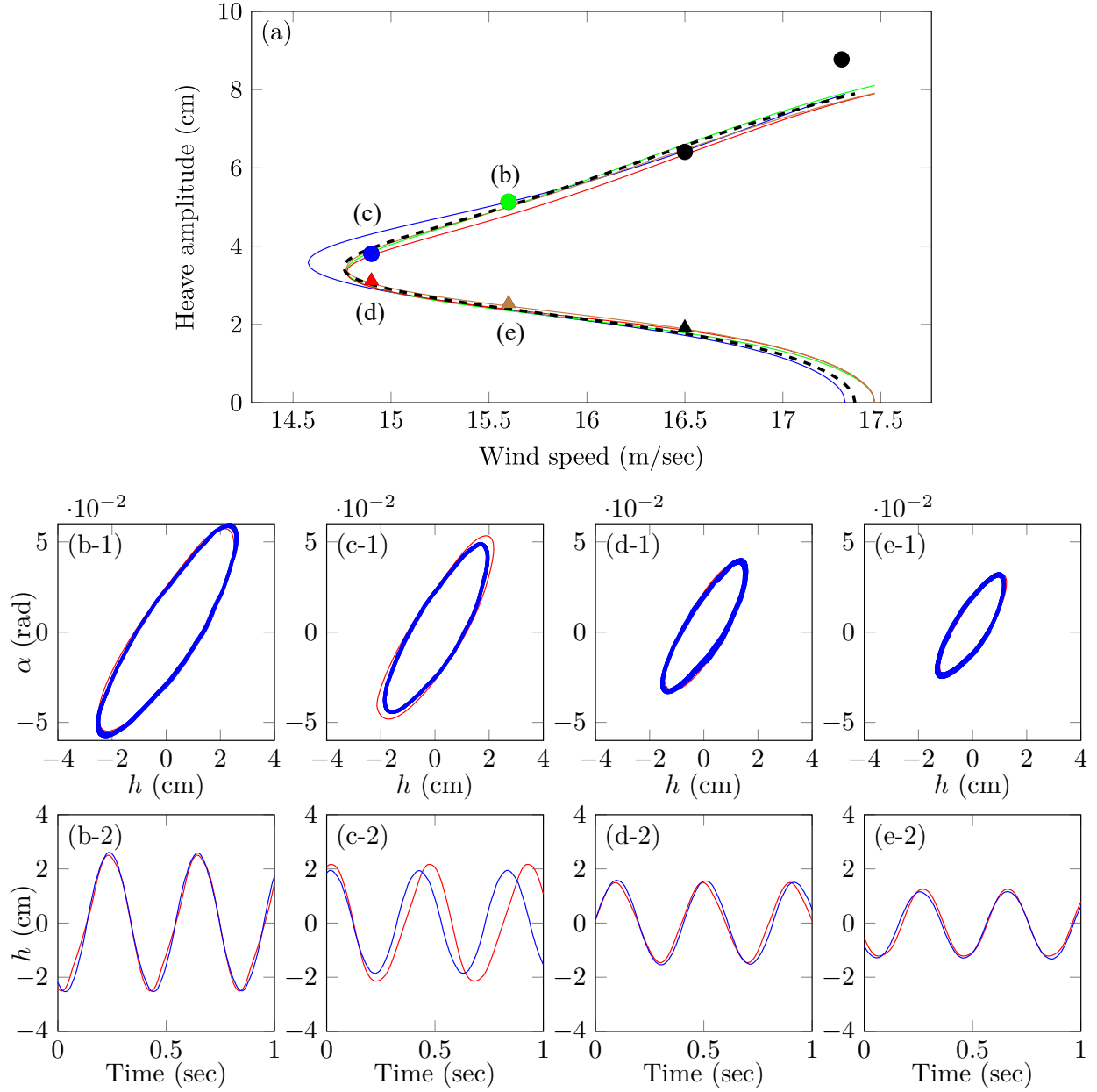


Figure 11: Effect of excluding one data point from the training data set on the hybrid M/ML model accuracy. (a) Bifurcation diagrams obtained when removing the data point of the same colour. For instance, the blue bifurcation curve is obtained with the model trained with a data set excluding the blue point. (—) Bifurcation diagram obtained from a model trained with all measured data. (b-1) – (e-1) Prediction of phase portrait at the excluded data point. (b-2) – (e-2) Prediction of time series at the excluded data point.

in Fig. 10, were also found to result in poorly- or even non-invertible transformations.



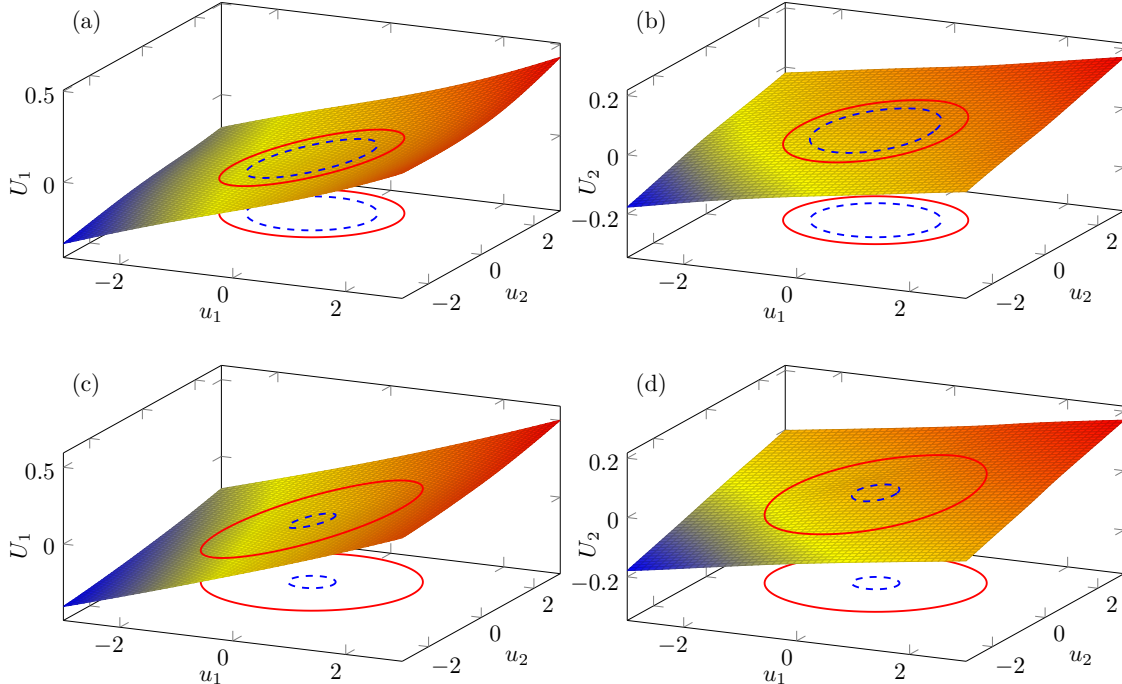


Figure 12: Mapping  $\mathbf{U}_{12}(\mathbf{u}, \mu) = (U_1(\mathbf{u}, \mu), U_2(\mathbf{u}, \mu))$  between normal form and physical coordinates. (a)  $U_1$  at  $\mu=15.0$  m/sec, (b)  $U_2$  at  $\mu=15.0$  m/sec, (c)  $U_1$  at  $\mu=17.0$  m/sec and (d)  $U_2$  at  $\mu=17.0$  m/sec.

## 6 Conclusions

In this paper, we have proposed a new hybrid modelling approach for physical systems with a Hopf bifurcation. At its core, it uses a mechanistic model, in the form of a normal-form-like model, to capture the phenomenology of the physical system. A data-driven, machine-learned model is then used to map the mechanistic model predictions onto the measured data. Our method was first demonstrated with numerical data collected on a Van der Pol oscillator and an aeroelastic model, and then with experimental data collected on aeroelastic rig during wind tunnel tests. The hybrid mechanistic/machine-learned models obtained with our method were shown to quantitatively capture the bifurcation diagrams of the different systems as well as their time evolution, even in the presence of multiple time-scales and noise.

The proposed method has several advantages such as being data-driven whilst also being able to work with a limited number of measured states and data. It also requires only the knowledge of the bifurcation structure of the system and is thus applicable to any system with a Hopf bifurcation. Replacing the current mechanistic model by a more detailed model of the physical system could improve the accuracy of the obtained model while also simplifying the training of the mapping. However, this would come at the cost of having a more application-specific modelling methodology. A more systematic approach to handle overfitting during ML model training is also required to make the method more systematically applicable. As the model is derived using LCO data only, the obtained hybrid mechanistic/machine-learned model reproduces the long-term behaviour of the physical system but is generally unable to accurately capture its transient dynamics. Future work should look at including transient data in the modelling approach. Finally, the principles of the proposed method are extremely general and could therefore be applied to systems with other types of bifurcations by changing the mechanistic model.

The hybrid mechanistic/machine-learned models obtained with our method can have multiple uses. The machine-learned part of the model could be exploited to improve understanding about the physical system of interest and provide new insights into the derivation of more accurate mechanistic models. The ability of the proposed models to reproduce the unstable part of the bifurcation diagram has also the potential help analyse stability boundaries and basins of attraction of physical systems, or help in reducing the cost of experimental methods such as CBC. Finally, the hybrid mechanistic/machine-learned models developed here

establish a rigorous framework to combine known physics with experimental and/or operational data and could therefore be used as digital twins for nonlinear systems.

## Statements

### Funding

This work was supported by a PhD Scholarship from the University of Bristol, the EPSRC (EP/K032738/1) and the Royal Academy of Engineering (RF1516/15/11).

### Data Availability

The datasets generated during and/or analysed during the current study are available in [https://github.com/KyoungHyunLee/ML\\_Hopf](https://github.com/KyoungHyunLee/ML_Hopf).

## References

- [1] Dimitriadis G. Introduction to Nonlinear Aeroelasticity. John Wiley & Sons; 2017.
- [2] Beregi S, Takacs D, Stepan G. Bifurcation analysis of wheel shimmy with non-smooth effects and time delay in the tyre-ground contact. *Nonlinear Dynamics*. 2019;98(1):841-58.
- [3] Kalmár-Nagy T, Stépán G, Moon FC. Subcritical Hopf bifurcation in the delay equation model for machine tool vibrations. *Nonlinear Dynamics*. 2001;26(2):121-42.
- [4] Adimy M, Crauste F, Ruan S. Stability and Hopf bifurcation in a mathematical model of pluripotent stem cell dynamics. *Nonlinear Analysis: Real World Applications*. 2005;6(4):651-70.
- [5] Guo S, Huang L. Hopf bifurcating periodic orbits in a ring of neurons with delays. *Physica D: Nonlinear Phenomena*. 2003;183(1-2):19-44.
- [6] Kuznetsov YA. Elements of applied bifurcation theory. vol. 112. Springer Science & Business Media; 2013.
- [7] Winkler DA, Le TC. Performance of deep and shallow neural networks, the universal approximation theorem, activity cliffs, and QSAR. *Molecular informatics*. 2017;36(1-2):1600118.
- [8] Wang S, Teng Y, Perdikaris P. Understanding and mitigating gradient flow pathologies in physics-informed neural networks. *SIAM Journal on Scientific Computing*. 2021;43(5):A3055-81.
- [9] Rasmussen CE. Gaussian processes in machine learning. In: Summer school on machine learning. Springer; 2003. p. 63-71.
- [10] Kim J, Lee K, Lee D, Jin SY, Park N. DPM: A Novel Training Method for Physics-Informed Neural Networks in Extrapolation. *Comput Phys*. 2019;378:686-707.
- [11] Raissi M, Perdikaris P, Karniadakis GE. Physics-informed neural networks: A deep learning framework for solving forward and inverse problems involving nonlinear partial differential equations. *Journal of Computational Physics*. 2019;378:686-707.
- [12] Raissi M, Perdikaris P, Karniadakis GE. Machine learning of linear differential equations using Gaussian processes. *Journal of Computational Physics*. 2017;348:683-93.
- [13] Raissi M, Perdikaris P, Karniadakis GE. Inferring solutions of differential equations using noisy multi-fidelity data. *Journal of Computational Physics*. 2017;335:736-46.
- [14] Rackauckas C, Ma Y, Martensen J, Warner C, Zubov K, Supekar R, et al. Universal differential equations for scientific machine learning. *arXiv preprint arXiv:200104385*. 2020.

- [15] Beregi S, Barton DA, Rezgui D, Neild SA. Using scientific machine learning for experimental bifurcation analysis of dynamic systems. arXiv preprint arXiv:211011854. 2021.
- [16] Sieber J, Krauskopf B. Control based bifurcation analysis for experiments. *Nonlinear Dynamics*. 2008;51(3):365-77.
- [17] Renson L, Shaw A, Barton D, Neild S. Application of control-based continuation to a nonlinear structure with harmonically coupled modes. *Mechanical Systems and Signal Processing*. 2019;120:449-64.
- [18] Renson L, Gonzalez-Buelga A, Barton D, Neild S. Robust identification of backbone curves using control-based continuation. *Journal of Sound and Vibration*. 2016;367:145-58.
- [19] Barton DA. Control-based continuation: Bifurcation and stability analysis for physical experiments. *Mechanical Systems and Signal Processing*. 2017;84:54-64.
- [20] Barton DA, Sieber J. Systematic experimental exploration of bifurcations with noninvasive control. *Physical Review E*. 2013;87(5):052916.
- [21] de Cesare I, Salzano D, di Bernardo M, Renson L, Marucci L. Control-Based Continuation: A New Approach to Prototype Synthetic Gene Networks. *ACS Synthetic Biology*, in press. 0;0(0):null.
- [22] Beregi S, Barton DA, Rezgui D, Neild SA. Improving robustness to noise of nonlinear parameter identification using control-based continuation. arXiv preprint arXiv:200111008. 2020.
- [23] Carr J. Applications of centre manifold theory. vol. 35. Springer Science & Business Media; 2012.
- [24] Rosenfeld A. Digital picture processing. Academic press; 1976.
- [25] Zhang D, Lu G. Review of shape representation and description techniques. *Pattern recognition*. 2004;37(1):1-19.
- [26] Zahn CT, Roskies RZ. Fourier descriptors for plane closed curves. *IEEE Transactions on computers*. 1972;100(3):269-81.
- [27] Penrose R. A generalized inverse for matrices. In: *Mathematical proceedings of the Cambridge philosophical society*. vol. 51. Cambridge University Press; 1955. p. 406-13.
- [28] Kanagawa M, Hennig P, Sejdinovic D, Sriperumbudur BK. Gaussian processes and kernel methods: A review on connections and equivalences. arXiv preprint arXiv:180702582. 2018.
- [29] Lin H, Jegelka S. Resnet with one-neuron hidden layers is a universal approximator. In: *Advances in neural information processing systems*; 2018. p. 6169-78.
- [30] Paszke A, Gross S, Massa F, Lerer A, Bradbury J, Chanan G, et al. Pytorch: An imperative style, high-performance deep learning library. In: *Advances in neural information processing systems*; 2019. p. 8026-37.
- [31] Innes M. Flux: Elegant machine learning with Julia. *Journal of Open Source Software*. 2018;3(25):602.
- [32] Da K. A method for stochastic optimization. arXiv preprint arXiv:14126980. 2014.
- [33] Liu DC, Nocedal J. On the limited memory BFGS method for large scale optimization. *Mathematical programming*. 1989;45(1-3):503-28.
- [34] Zhang H, Abhyankar S, Constantinescu E, Anitescu M. Discrete adjoint sensitivity analysis of hybrid dynamical systems with switching. *IEEE Transactions on Circuits and Systems I: Regular Papers*. 2017;64(5):1247-59.
- [35] Lauß T, Oberpeilsteiner S, Steiner W, Nachbagauer K. The discrete adjoint method for parameter identification in multibody system dynamics. *Multibody system dynamics*. 2018;42(4):397-410.

- [36] Ruder S. An overview of gradient descent optimization algorithms. arXiv preprint arXiv:160904747. 2016.
- [37] Fletcher R. Practical methods of optimization. John Wiley & Sons; 2013.
- [38] Abdelkefi A, Vasconcellos R, Nayfeh AH, Hajj MR. An analytical and experimental investigation into limit-cycle oscillations of an aeroelastic system. *Nonlinear Dynamics*. 2013;71(1-2):159-73.
- [39] Lee K, Tartaruga I, Rezgui D, Renson L, Neild SA, Barton DAW. Analysis of self-excited flutter oscillations with control-based continuation. Preprint. 2022.
- [40] Lee K, Barton D, Renson L. Reduced-order modelling of flutter oscillations using normal forms and scientific machine learning. arXiv e-prints. 2020:arXiv-2011.
- [41] Barton DAW. Real-time control hardware/software based on the BeagleBone Black; 2015. Available from: <http://github.com/~dawbarton/rtc>.
- [42] Louizos C, Welling M, Kingma DP. Learning sparse neural networks through  $L_0$  regularization. arXiv preprint arXiv:171201312. 2017.
- [43] Burden F, Winkler D. Bayesian regularization of neural networks. *Artificial neural networks*. 2008:23-42.